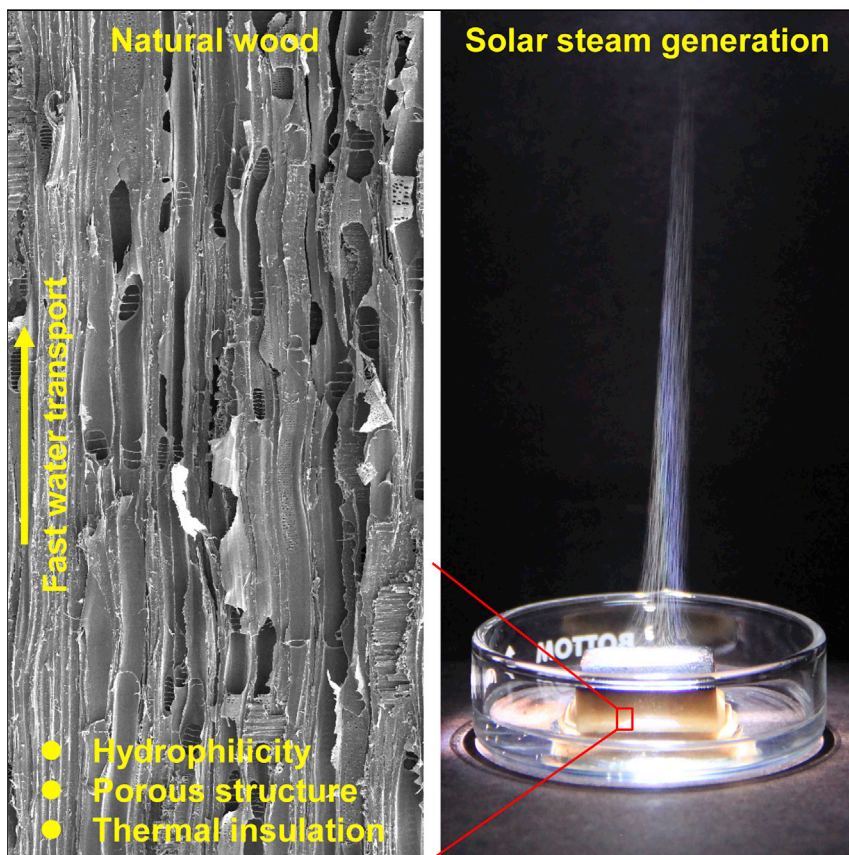


Article

Rich Mesostructures Derived from Natural Woods for Solar Steam Generation



Chao Jia, Yiju Li, Zhi Yang, ...,
Bao Yang, Siddhartha Das,
Liangbing Hu

binghu@umd.edu

HIGHLIGHTS

Natural wood materials possess aligned microchannels and cellulose nanofibers

Favorable hydrophilicity and high porosity result in fast water transport in wood

Carbonized natural wood enables high-efficiency solar steam generation

Low thermal conductivity can confine heat on the surface of carbonized wood

All-in-one wood-based solar steam generation devices were prepared by directly carbonizing the top surface of natural wood materials. High solar steam generation efficiencies were achieved by virtue of the excellent hydrophilicity, low thermal conductivity, interconnected porous network, and improved light absorption capability, demonstrating the great potential of natural wood in energy-water nexus applications.

Jia et al., *Joule* 1, 588–599
November 15, 2017 © 2017 Elsevier Inc.
<https://doi.org/10.1016/j.joule.2017.09.011>

Article

Rich Mesostructures Derived from Natural Woods for Solar Steam Generation

Chao Jia,^{1,3} Yiju Li,^{1,3} Zhi Yang,² Guang Chen,² Yonggang Yao,¹ Feng Jiang,¹ Yudi Kuang,¹ Glenn Pastel,¹ Hua Xie,¹ Bao Yang,² Siddhartha Das,² and Liangbing Hu^{1,4,*}

SUMMARY

A tree is a living energy-water system. Intensive study of tree-derived natural wood is of great significance for the sustainable development of human civilization and reduced dependence on nonrenewable resources. Here, we report on the mesostructures of several natural wood materials as well as their thermal conductivities and mechanical properties. We found that natural wood, including hardwood and softwood, possesses excellent hydrophilicity, an interconnected pore network, low thermal conductivity, and various mechanical properties. Inspired by the critical ecological energy-water nexus, high-efficiency solar steam generation based on natural wood is demonstrated in this work. The variation in multiple natural wood microstructures results in significantly different solar steam generation performances, with the more porous wood showing higher evaporation efficiency based on our results. The inherent rich mesostructures, aligned microchannels, and favorable hydrophilicity enable natural wood materials to be applied in many other fields of the energy-water nexus.

INTRODUCTION

Our earth possesses rich forest resources, covering almost 30% of the continental landmass, and trees play a vital role in maintaining the ecological balance of our planet. As a living energy-water system, trees can convert sunlight into chemical energy and synthesize carbohydrate molecules using carbon dioxide and water by photosynthesis. This process is a critical ecological energy-water nexus. The transport of water in trees is critical for the photosynthesis process, and can be achieved by virtue of the rich mesoporous structure, vertically aligned microchannels, and a bordered pits system. Wood from trees is the fifth most important trade product worldwide and has been used ubiquitously in every aspect of human life, including buildings, furniture, chemical products, food, and textile products.¹

Based on the differences in microstructure, wood can be classified into two kinds: hardwood with fiber tracheids and vessel elements and softwood with only tracheids.² Microfibrils are distributed within the cell walls,¹ while cellulose nanofibrils and nanocrystals can be further isolated from microfibrils through mechanical,³ chemical,^{4–7} or enzymatic treatment.^{8,9} Looking further into the chemical composition, wood is a biopolymer composite, mainly made of cellulose, hemicellulose, and lignin. Owing to the variations in the above-mentioned hierarchical structures, different wood species show different densities, porosities, thermal conductivities, and mechanical properties, thereby providing tunable functionalities that can be utilized in various applications.

Apart from the above-mentioned conventional applications, wood has been explored and applied in some emerging areas, such as transparent materials,^{10,11}

Context & Scale

A tree is a living energy-water system that can convert solar energy into chemical energy and synthesize carbohydrate molecules using carbon dioxide and water by photosynthesis. Intensive study of tree-derived natural wood is of great significance for the sustainable development of human civilization and reduced dependence on nonrenewable resources. Natural wood, including hardwood and softwood, possesses excellent hydrophilicity, an interconnected pore network, and low thermal conductivity. Inspired by the critical ecological energy-water nexus, an efficient solar steam generation device was demonstrated by directly carbonizing the top surface of natural wood. High light absorption and effective photothermal conversion in the carbonized layer, together with fast water transport and evaporation, result in high solar steam generation efficiency. The success with solar steam generation will spark many further studies about energy-water nexus applications based on natural wood.

water treatment,¹² energy storage,¹³ electronic devices,^{14–16} building materials,¹⁷ and composites.¹⁸ The intriguing mesostructures and fast water transport capability of wood inspired us to mimic natural trees and apply wood in an artificial energy-water nexus. Efficient solar steam generation was demonstrated as a proof of concept in this work. Solar steam generation has become a particularly attractive energy-efficient method for fresh water production due to the low environmental impact and sustainability of solar-based devices.^{19–28} Wood shows many advantages for application in solar steam generation devices, for instance, good hydrophilicity, lightweight structure, inherent microchannels for water transport, and excellent thermal insulation. Here, several hardwoods and softwoods were studied and compared, and their similarities and differences were clarified. Wood-based solar steam generation devices (SSGDs) were obtained through a facile one-step carbonization of the top surface of natural wood samples. We demonstrated that devices from different wood species show an enormous difference in solar steam generation efficiency. The energy conversion efficiency of the poplar wood-based solar steam generation device with a porosity of 66% is as high as 86.7% under an intensity of 10 kW m^{-2} . Given the merits of the inherent rich mesostructures along with the potential for functionalization, natural wood materials are fascinating for energy-water nexus applications.

RESULTS

Composition, Mesostructure, and Density of Natural Wood

Wood is mainly composed of cellulose, hemicellulose, and lignin, which account for 40%–50%, ~25%, and 25%–35% of the dry weight of wood, respectively (Figure 1A).¹ Cellulose is made of repeating β -D-glucopyranose units that are covalently linked by (1 \rightarrow 4) glycosidic bonds. The degree of polymerization (indicated as “n” in the molecular structure) of wood cellulose molecular chains is about 10,000 glucose monomer units (Figure 1B).²⁹ Hemicellulose is a heterogeneous group of polysaccharides composed of xyloglucans, xylans, mannans and glucomannans, and β -(1 \rightarrow 3, 1 \rightarrow 4)-glucans, which strengthen the cell walls through interactions with cellulose and lignin (Figure 1B).³⁰ Lignin, the second most abundant biopolymer on earth, is a complex phenolic polymer, which plays an important role in maintaining the integrity of the cell structure and stem strength.³¹ Lignin is derived from the polymerization of three types of monolignols: *p*-coumaryl alcohol, coniferyl alcohol, and sinapyl alcohol (Figure 1B), which form *p*-hydroxyphenyl (H), guaiacyl (G), and syringyl (S) units, respectively.³² In the three major components of wood, cellulose and hemicellulose contain a large number of hydroxyl groups and are highly hydrophilic, which leads to excellent hydrophilicity of the cell walls and overall structure (Figure S1).

Wood can be divided into hardwood and softwood based on its physical structure and composition. Hardwood consists of three kinds of cells, i.e., fiber tracheids, vessel elements, and parenchyma. The fiber tracheids with a honeycomb-like structure provide structural support, while the vessels with a larger lumen diameter are used for water transport. Softwood is primarily composed of highly elongated tracheids and parenchyma, where tracheids have the function of providing mechanical support and transferring fluids throughout the wood.²

In spite of their structural differences, both hardwood and softwood have inherent hierarchical structures, with vertically aligned microchannels for transporting water, ions, and other nutrients (Figure 1C). This hydrophilic and porous structure of natural wood plays an important role in efficiently transporting water from the roots to the leaves of the tree by virtue of capillary action. In addition, the structural differences in

¹Department of Materials Science and Engineering, University of Maryland, College Park, MD 20742, USA

²Department of Mechanical Engineering, University of Maryland, College Park, MD 20742, USA

³These authors contributed equally

⁴Lead Contact

*Correspondence: binghu@umd.edu

<https://doi.org/10.1016/j.joule.2017.09.011>

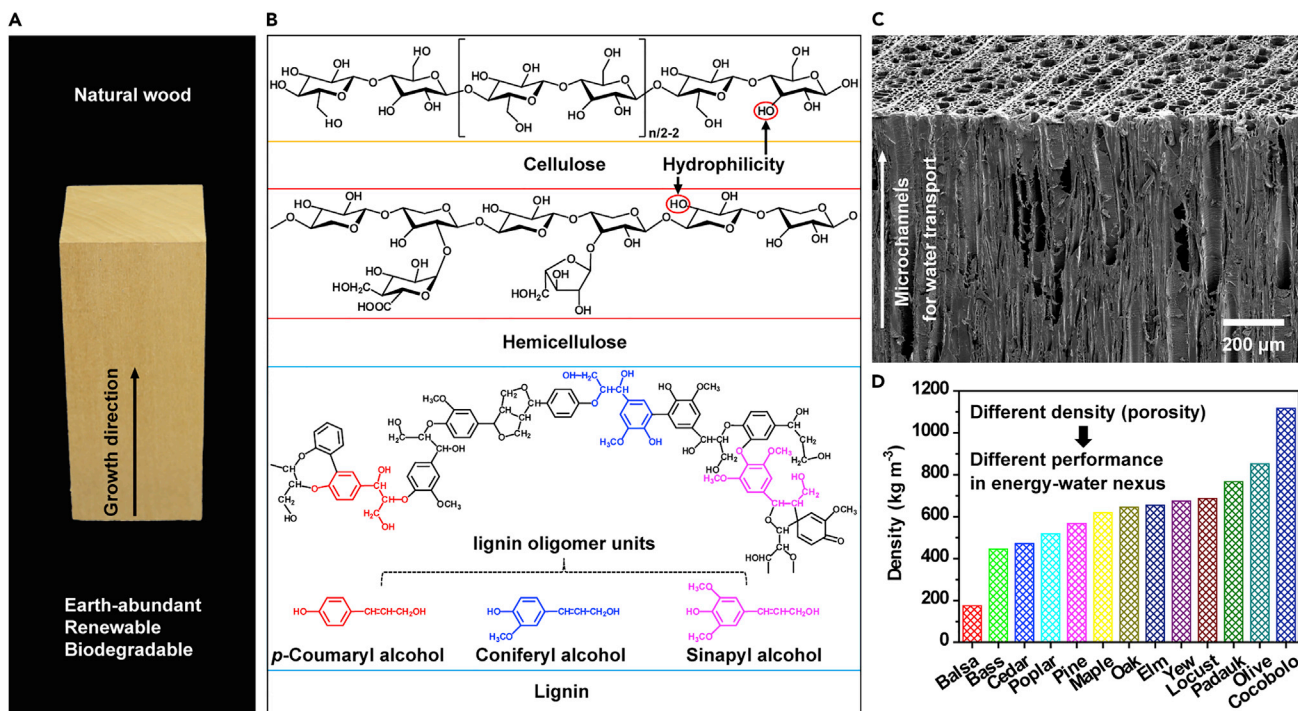


Figure 1. Composition, Mesostructure, and Density of Natural Wood

(A) Digital image of a wood block. Note that wood is an earth-abundant, renewable, and biodegradable biomaterial.

(B) Molecular structures of cellulose, hemicellulose, and lignin, the three main components of wood (*n* is the degree of polymerization).

(C) SEM image of natural wood to show the mesostructure, where the vertically aligned microchannels on the longitudinal direction and micrometer-sized pores on the cross-section can be clearly seen. Scale bar, 200 μm .

(D) Density comparison of various natural woods. See also Figure S1.

wood also lead to other properties, the most obvious being the density of the wood. The wood density varies significantly with the species, ranging from 175 kg m^{-3} for the lightest balsa wood to more than $1,000 \text{ kg m}^{-3}$ for some kinds of sandalwood such as cocobolo wood (Figure 1D). The difference in densities is usually indicative of different porosities and affects the performance in energy-water nexus applications.

Natural Wood Materials Possess Aligned Microchannels, Cellulose Nanofibers, and Bordered Pits

Both hardwood and softwood have similar vertically aligned microchannels and interconnected pore networks, which enable water transport in energy-water nexus applications. Hardwoods come from broad-leaved trees, which are also known as angiosperms because their seeds are enclosed in fruits or pods. Typical hardwoods include balsa (Figure S2), bass (Figure S3), cocobolo (Figures 3C and S4), elm (Figure S5), locust (Figure S6), maple (Figure S7), oak (Figure S8), olive (Figures 3B and S9), padauk (Figure S10), and poplar wood (Figures 2A–2D, 3A, and S11). Softwoods, also known as gymnosperms, are from evergreen trees that have needles and cones year round, and include cedar (Figures 3D and S12), pine (Figures 2E–2H, 3E, and S13), and yew wood (Figures 3F and S14). Hardwoods possess a more complex structure than softwoods and often grow more slowly as a result. Figures 2A and 2E are digital images of a typical hardwood, poplar wood, and a typical softwood, pine wood, respectively. The representative scanning electron microscopy (SEM) images of their longitudinal sections reveal the porous structures (Figures 2B and 2F). The significant characteristic differentiating hardwood from

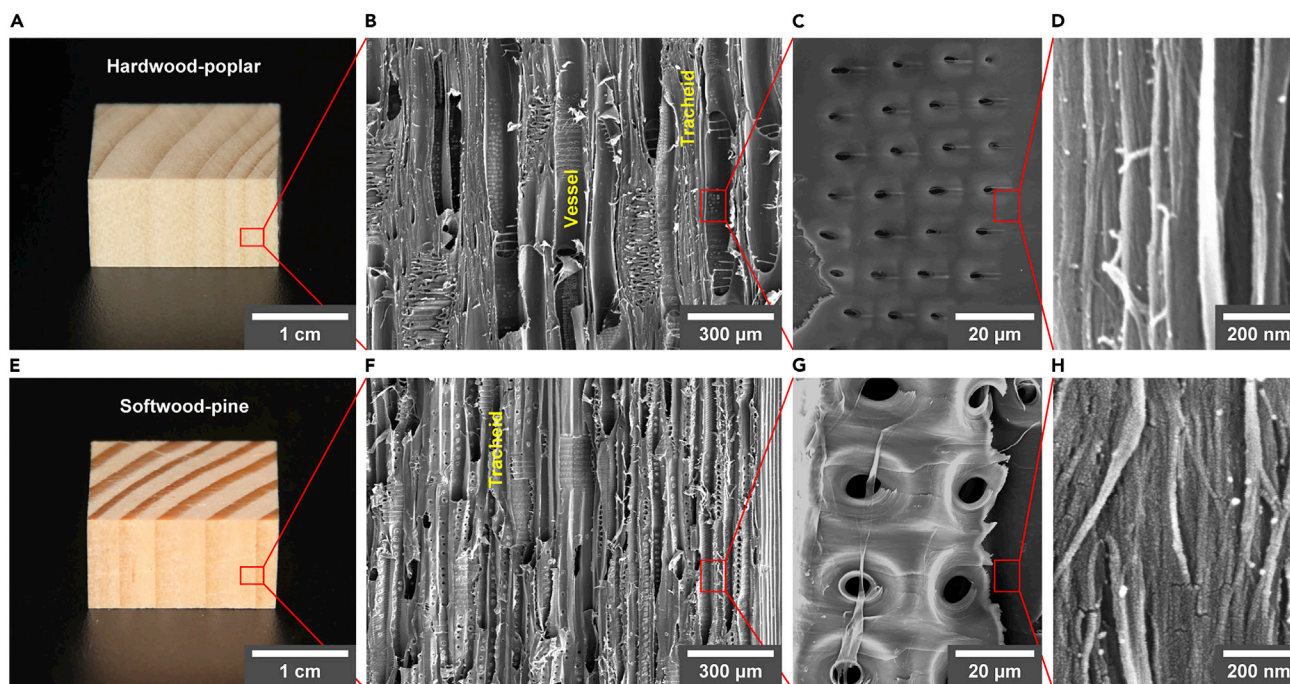


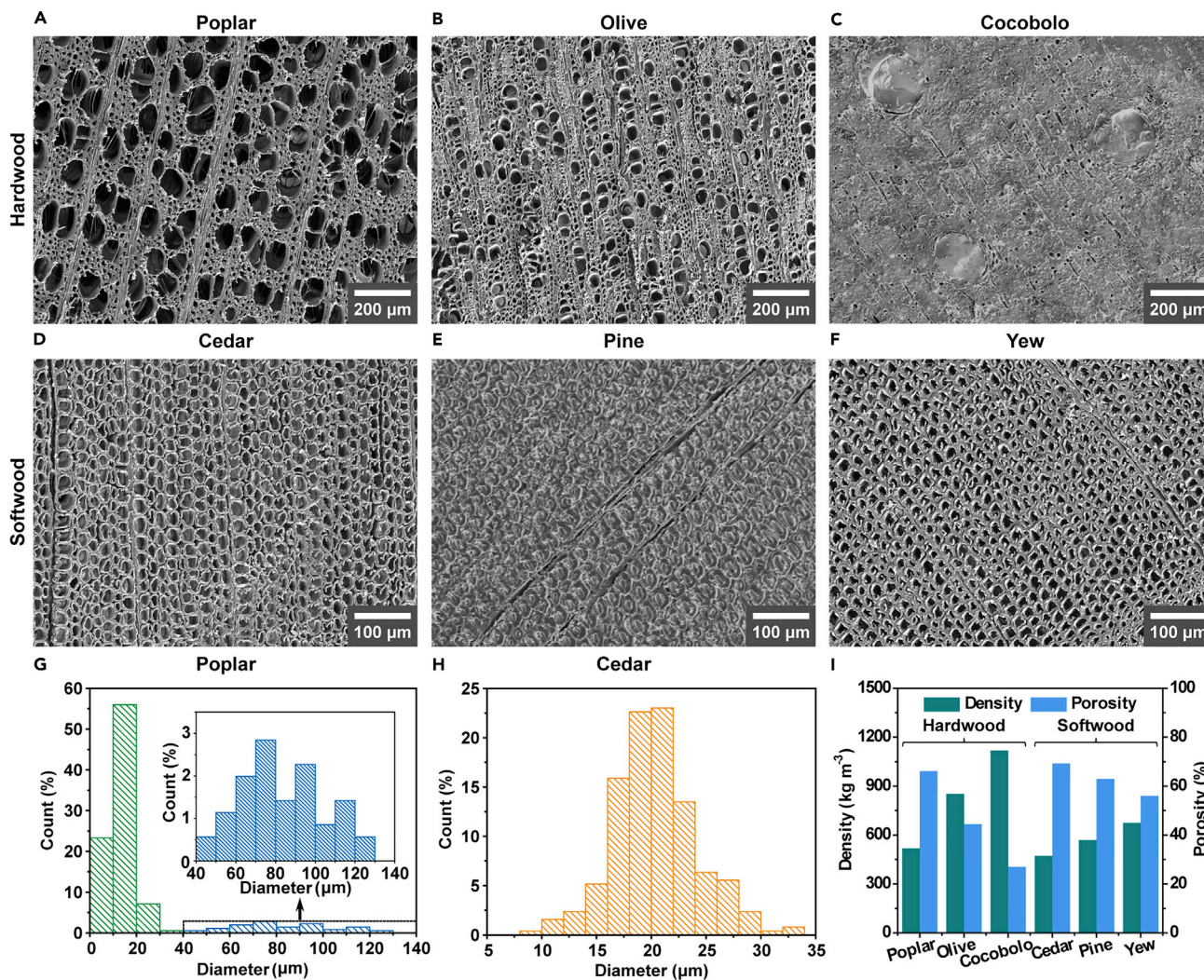
Figure 2. Mesostructure Comparison of Hardwood and Softwood

Digital images of (A) poplar wood, a typical hardwood and (E) pine wood, a typical softwood. SEM images of (B) poplar wood and (F) pine wood to show the vertically aligned microchannels. High-magnification SEM images of the microchannels in (C) poplar wood and (G) pine wood to show the existence of the pits responsible for transverse water transfer. High-magnification SEM images of the microchannels in (D) poplar wood and (H) pine wood to show the aligned cellulose nanofibers. Scale bars: (A and E) 1 cm; (B and F) 300 μm ; (C and G) 20 μm ; (D and H) 200 nm. See also [Figures S2–S14](#).

softwood is the existence of vessel elements ([Figure 2B](#)). Vessels in hardwood have a large lumen diameter and are connected by perforation plates at the cell ends to function as the main pathways for water transport. The fiber tracheids with a smaller lumen diameter are interconnected through pits and mainly used for structural support ([Figures 2B and 2C](#)). However, softwood only has highly elongated tracheids, which not only provide mechanical support, but can also transfer water through the bordered pits ([Figures 2F and 2G](#)). In addition, both hardwood and softwood are composed of aligned cellulose nanofibers ([Figures 2D and 2H](#)), which are responsible for the high strength of natural wood.

The Different Pore Diameters and Porosity of Hardwood and Softwood

Porosity is another critical property of materials in energy-water nexus applications.^{12,20,21,33} Wood materials have porous structures, and their porosity depends on the wood species. [Figures 3A–3C](#) display the top view SEM images of different hardwoods, including poplar, olive, and cocobolo wood, and obvious differences in lumen diameter can be clearly seen. In addition, for hardwoods, the vessels and fiber tracheids also exhibit different lumen diameters, which correspond to the two peaks in the pore diameter distribution ([Figure 3G](#)). Compared with hardwood, softwood possesses homogeneous pores, as shown in [Figures 3D–3F](#). For example, in [Figure 3H](#), a softwood such as cedar wood only has one distinguishing peak in the pore diameter distribution, which corresponds to the tracheids. The different pore size results in different density and porosity ([Figures 3I and S15](#)). [Figure 3I](#) presents the densities of different hardwoods and shows the significant differences. Cocobolo wood has a density of $1,118 \text{ kg m}^{-3}$, higher than that of water. Poplar wood shows a density of 518 kg m^{-3} , roughly two times smaller than that of cocobolo



wood, resulting in a high porosity of 66%. Smaller differences in density and porosity are observed for different softwoods, revealing their more uniform structures.

Natural Wood Materials Demonstrate Low Thermal Conductivity

The anisotropic structure of wood leads to different thermal conductivities in different directions. Figures 4A and 4C show the schematics of a wood block with vertical channels (referred to as L wood) and a wood block with horizontal channels (referred to as R wood), respectively. The thermal conductivities of different original woods, including poplar, pine, and cocobolo wood, were measured using a Steady State Laser-Infrared Camera Thermal Conductivity Characterization System (Figure S16, see Supplemental Information for experimental details). The thermal conductivity data were obtained experimentally and from ANSYS numerical

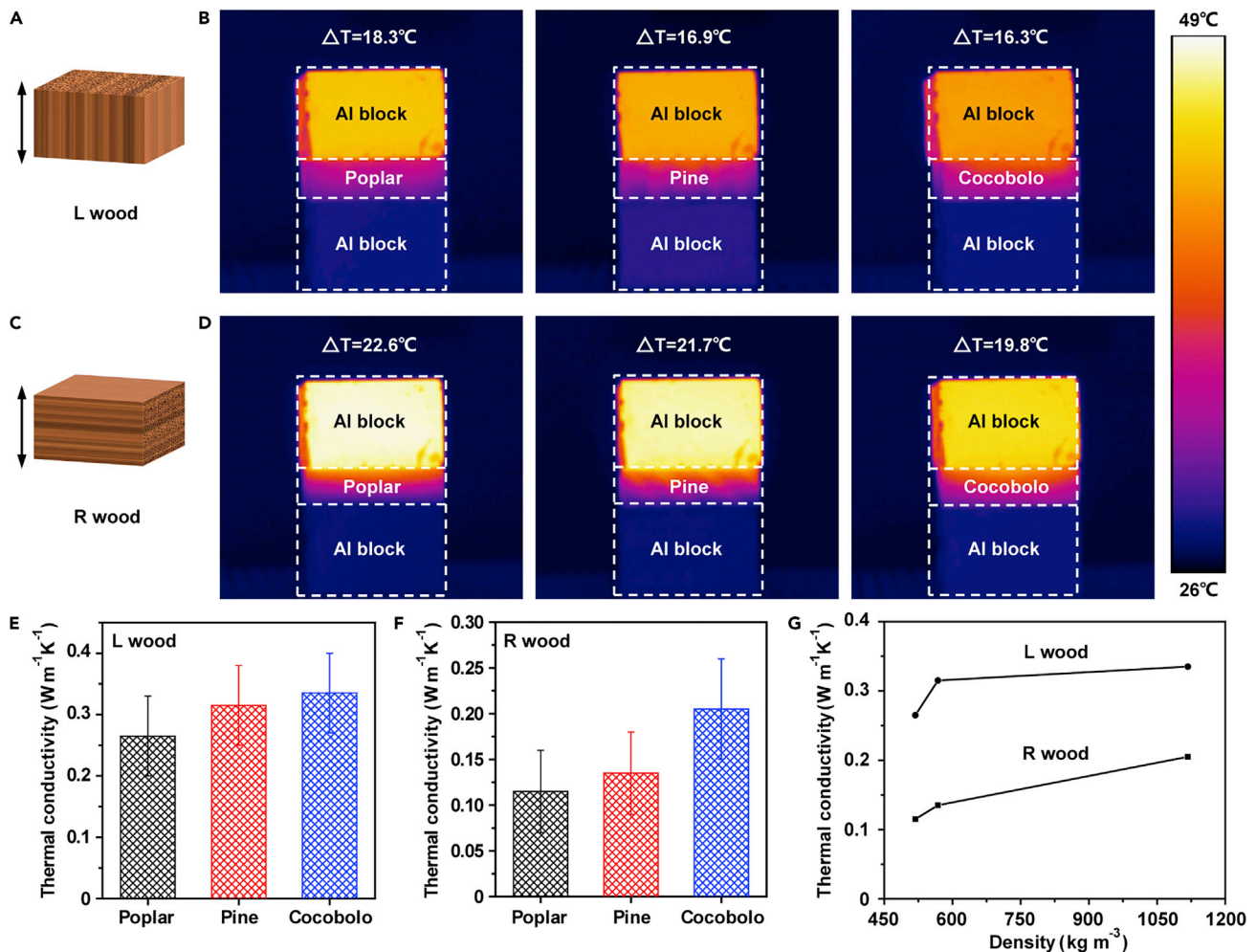


Figure 4. Thermal Conductivity Characterization of Natural Poplar, Pine, and Cocobolo Wood

(A and B) Schematic (A) and infrared images (B) of different L woods.

(C and D) Schematic (C) and infrared images (D) of different R woods. The arrows show the thermal conduction direction. ΔT is the temperature difference of top and bottom surface of the wood samples.

(E and F) Thermal conductivity of different L woods (E) and R woods (F). Data are presented as the mean with error bars.

(G) Relationship between thermal conductivity and wood density.

See also Figures S16–S18.

simulation based on the temperature difference (ΔT) between the top and bottom surface of the wood samples (Figures 4B and 4D, and S17). The thermal conductivities of poplar, pine, and cocobolo L wood in the dry state are 0.27, 0.32, and 0.34 $\text{W m}^{-1} \text{K}^{-1}$, respectively (Figure 4E), higher than that of the corresponding R wood of 0.12, 0.14, and 0.21 $\text{W m}^{-1} \text{K}^{-1}$ (Figure 4F), respectively, in agreement with previous research.³⁴ We also explored the relationship of thermal conductivity and wood density and found that the thermal conductivity increases with wood density for both directions (Figure 4G). Figures S18A and S18B present the tensile stress-strain curves of natural poplar, pine, and cocobolo wood. As expected, the woods also demonstrate anisotropic mechanical properties in different directions. Compared with R wood, all the L woods exhibit higher mechanical strength, with tensile strengths of 57.2, 26.1, and 105.3 MPa for natural poplar, pine, and cocobolo wood, respectively (Figure S18C). Note that the tensile strength of natural poplar, pine, and cocobolo R wood is only 6.9, 3.8, and 8.7 MPa, respectively (Figure S18D).

The mechanical strength of the selected wood materials is much higher than that of some reported materials used in energy-water nexus applications.³⁵

Carbonized Wood Enables High-Efficiency Solar Steam Generation

By virtue of the intriguing mesostructures and fast water transport, wood materials have been used for extensive energy-water nexus applications, including membrane filters¹² and solar steam generation.^{21,22} Recently, Zhou et al.²² reported that natural wood can be employed as a solar absorber after pretreatment, polishing, alcohol flame treatment, and cold-water quenching. The preparation procedure is complicated and time consuming, which limits its feasibility for large-scale production. Moreover, the effects of the natural wood mesostructures on solar steam generation performance were not studied. In this study, we facilely carbonized various natural wood species and compared their root properties against the resultant solar steam generation performance.

The performance of SSGDs is mainly determined by four structural characteristics, i.e., light absorption on the surface, thermal insulation, hydrophilicity, and the interconnected porous structure for water transport.³⁶ Natural wood with excellent hydrophilicity, low thermal conductivity, and interconnected porous network is an ideal candidate for high-efficiency solar steam generation. Here, all-in-one wood-based SSGDs were prepared by directly carbonizing the top surface of poplar, pine, and cocobolo L wood to improve the absorption efficiency of solar irradiance. Compared with other preparation methods for SSGDs,^{21,22} our reported fabrication process for wood-based SSGDs is quite simple and cost-effective. The top surface of the natural wood samples are carbonized at 500°C for 60 s on a hot plate. After carbonization, the top surface of the wood samples becomes more porous (Figure S19), which is beneficial to water transport and light absorption during solar steam generation.

We measured the specific weight of different wood-based SSGDs before and after absorbing water to evaluate the water-absorbing properties (Figure 5A). As expected, the higher the porosity, the more water absorption observed. Because the density of cocobolo wood is higher than water, it cannot float on water. During solar steam generation measurements, we fixed the cocobolo wood-based SSGD on the surface of the water reservoir to keep it from sinking. The light transmittance and reflectance spectra of wood-based SSGDs were measured by a UV-visible spectrophotometer equipped with an integrating sphere in the wavelength range of 250–2,500 nm, and the absorption spectrum was calculated based on the transmittance and reflectance spectra (Figures 5B, S20, and S21). Note that the absorption of the carbonized wood samples increases with increasing carbonization time. For comparison, the solar steam generation performance of wood samples carbonized for 60 s was collected. As shown in Figure 5B, the total absorption across the 250–2,500 nm wavelength spectra is 92%, 84%, and 96% for poplar, pine, and cocobolo wood-based SSGDs, respectively. Upon irradiation, the water can be evaporated rapidly with the appearance of steam over the wood-based SSGDs (Figure 5C).

The rate of solar steam generation of the wood-based SSGDs was quantitatively analyzed by determining the weight loss of water as a function of irradiation time. Since water will evaporate even under dark conditions when the relative humidity is lower than 100%, the dark field evaporation rate (ER) of the wood-based SSGDs was measured (Figure S22) and subtracted from the subsequent solar steam measurements. Under irradiation intensity of 10 suns (10 kW m^{-2}), the rate of water evaporation of wood-based SSGDs increases with increasing irradiation time until reaching steady state after 30 min (Figure 5D). The steady-state ER of the poplar

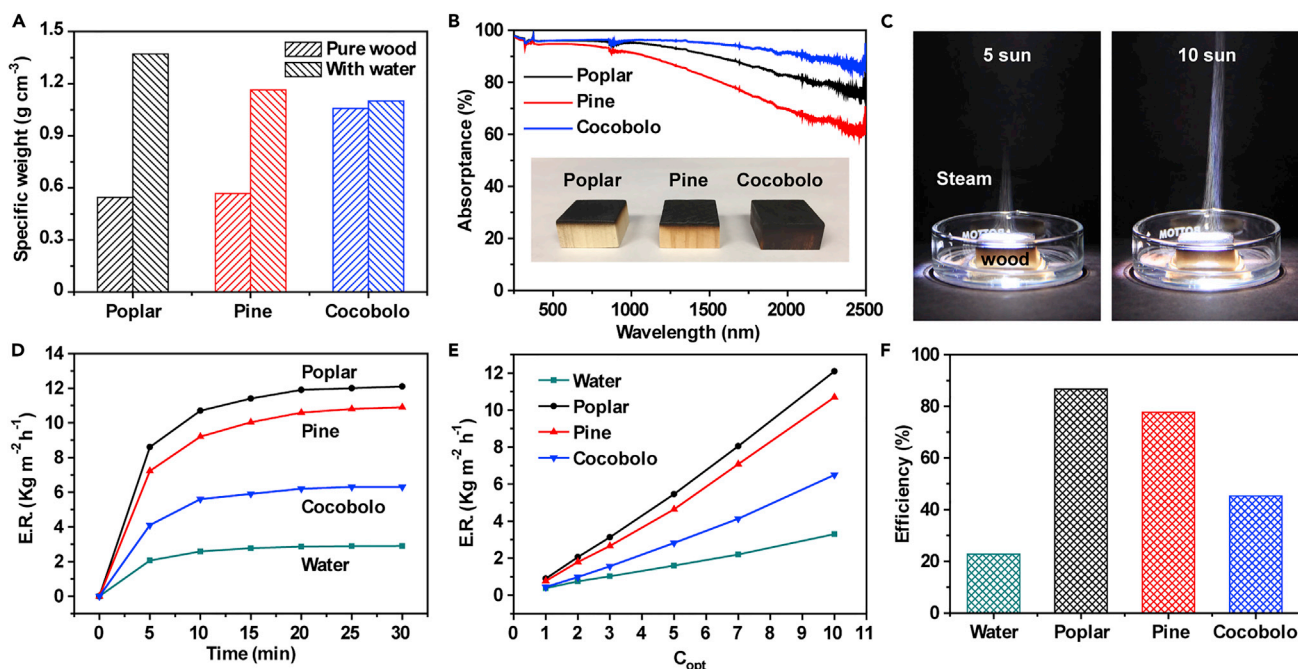


Figure 5. Solar Steam Generation of Different L Wood-Based SSGDs

(A) The specific weight of the different wood-based SSGDs with dimensions $2 \times 2 \times 1$ cm (length \times width \times height) before and after absorbing water. (B) Light absorption spectra of the different wood-based SSGDs. Inset: the digital image of three wood-based SSGDs. (C) Steam generation digital images of the wood-based SSGDs under light intensities of 5 and 10 suns. (D) The time dependence of the water evaporation rate (ER) for the different wood-based SSGDs and pure water at 10 suns. (E) The water evaporation rate of different wood-based SSGDs and pure water under different solar illumination ($1 C_{opt} = 1 \text{ kW m}^{-2}$). (F) Comparison of the efficiency of solar steam generation for the different wood-based SSGDs and pure water at 10 suns. See also Figures S19–S25.

wood-based SSGD is as high as $12.1 \text{ kg m}^{-2} \text{ hr}^{-1}$, nearly two times higher than that of the cocobolo wood-based SSGD under identical irradiation power density. In addition, the water ER of wood-based SSGDs increases with increasing irradiation intensity (Figure 5E). Note that the ERs of pure water under various solar intensities are much lower than that of the wood-based SSGDs. The irradiation time dependence of the surface temperature for poplar, pine, and cocobolo wood-based SSGDs in water under solar illumination of 10 suns was obtained (Figure S23). The surface temperature increases quickly after irradiation from ambient temperature ($\sim 20^\circ\text{C}$) to a constant temperature of approximately 92°C , 85°C , and 99°C for poplar, pine, and cocobolo wood-based SSGDs, respectively, in 10 min. The large temperature rise of 72°C , 65°C , and 79°C , respectively, results from the high light absorption of the carbonized layer together with effective light scattering in the microchannels. The highest temperature increase of the cocobolo wood-based SSGD can be ascribed to the higher density and light absorption of cocobolo wood. Compared with the pine wood-based SSGD, the poplar wood-based SSGD with a lower density showed a greater increase in temperature, which is attributed to the higher incident light absorption of the carbonized layer and the light-capturing capability of the wood microchannels.

The solar steam generation efficiency η was calculated based on the following equation:³⁶

$$\eta = \dot{m}h_{LV}/q_iC_{opt}$$

where \dot{m} is the ER under different irradiation intensities, h_{LV} denotes the total enthalpy of the liquid-vapor phase conversion, containing the sensible heat and phase conversion enthalpy, q_i is the nominal solar intensity (1 kW m^{-2}), C_{opt} is the multiple of 1-sun irradiation intensity. The steam generation efficiency of different wood-based SSGDs was compared under the power density of 10 suns (Figure 5F). The calculated evaporation efficiencies of poplar, pine, and cocobolo wood-based SSGDs are 86.7%, 76.3%, and 46.8%, respectively. The calculated conversion efficiency of pure water is only 22.8% under 10 suns, which is much lower than that of our wood-based SSGDs. In addition, the same results were obtained under 1 sun, but the solar steam generation efficiencies under 1 sun are lower than that under 10 suns for our wood-based SSGDs (Figure S24). Based on our results, the more porous wood shows higher efficiency. The significantly higher efficiency of the poplar wood-based SSGD can be rationalized as follows. Firstly, the higher porosity of poplar wood (66%) enables rapid water transport from the bulk water to the carbonized layer, thereby replenishing surface water evaporation (Figure 3I). Secondly, heat transfer from the carbonized layer of the poplar wood-based SSGD to the bulk water is minimized due to the low thermal conductivity of poplar wood ($0.27 \text{ W m}^{-1} \text{ K}^{-1}$) (Figure 4E). Lastly, the high light-capturing capability of the poplar wood-based SSGD can be achieved owing to the high porosity, resulting in efficient light absorption (Figure 5B).

DISCUSSION

The water evaporated by solar illumination from the top surface of wood-based SSGDs is continuously replenished by the capillary forces in the mesostructure of the SSGDs. Continuous evaporation is possible only when the flow rate at which this capillarity-driven water replenishment is more than or equal to the rate at which the water is lost due to evaporation from the top surface. The wood structure can be considered as arrays of microchannels and, according to Darcy's law, the flow rate through such a permeable medium is

$$Q = \frac{\kappa}{\mu} \frac{\Delta P}{T}, \quad (\text{Equation 1})$$

where Q is the flow rate per unit area, κ is the permeability of the wood, μ is the viscosity of the fluid, T is the thickness of the wood block (or length of the microchannels in wood), and ΔP is the equivalent pressure difference between the top and bottom sides of the wood block (or the two ends of the microchannels). Here, the relation between permeability κ , porosity ϕ , and the microchannel diameter d is

$$\kappa = \frac{\phi d^2}{32\tau}, \quad (\text{Equation 2})$$

where τ is the tortuosity of the microchannels. As the SSGD fills due to capillarity, the pressure difference ΔP is a combination of the surface tension driven pressure gradient and the hydrostatic pressure gradient. Therefore,

$$\Delta P = \frac{8\sigma \cos\theta}{d} - \rho g T, \quad (\text{Equation 3})$$

where the capillary driven pressure gradient is $8\sigma \cos\theta/d$ (σ is the air-water surface tension, θ is the contact angle at the air-wood-water three-phase contact line, d is the average diameter of the microcapillaries constituting the wood), ρ is the density of water, and g is the acceleration due to gravity. Using Equations (2) and (3) and considering the contact angle θ as zero, we can finally re-write Equation (1) as

$$Q = \frac{\phi d^2}{32\mu\tau} \left(\frac{8\sigma}{dT} - \rho g \right). \quad (\text{Equation 4})$$

For the wood block, $T = 0.01$ m, $d \sim 10\text{--}100$ μm , $\sigma = 0.072$ N m⁻¹, $\rho = 1,000$ kg m⁻³, and $g = 9.8$ m s⁻², we have $8\sigma/dT \gg \rho g$. Under these conditions, the flow rate is expressed as:

$$Q = \frac{\phi d}{4\mu\tau} \frac{\sigma}{T}. \quad (\text{Equation 5})$$

Given the porosity (ϕ) and effective pore diameter (d) of poplar (66%, 80 μm), pine (63%, 32 μm), and cocobolo wood (27%, 16 μm) for water transport, we can use Equation (5) to establish:

$$Q_{\text{poplar}}:Q_{\text{pine}}:Q_{\text{cocobolo}} = 12:5:1. \quad (\text{Equation 6})$$

This comparison between the flow rates of pine and cocobolo wood can be seen in Figures 5D and 5E. The water transport capability of the poplar wood is much more efficient than both the pine and cocobolo wood. In fact, the water ascends rapidly in the poplar wood-based SSGD by capillary action to replenish the evaporated water and gushes to form a film of water on the top surface. Under these conditions, the ER is limited by the solar illumination. This illumination-limited evaporation is the reason why there is a much smaller difference between the ER of poplar and pine wood despite the difference in flow rates.

$$Q_{\text{poplar}}:Q_{\text{pine}} = 12:5.$$

Finally, we would like to point out that decreasing the thickness T of the wood block increases the effective capillarity-driven pressure gradient ($8\sigma/dT$), which in turn can be employed to increase the water transport rate in wood samples. As shown in Figure S25A, the ER gradually increases with incremental decreases in wood thickness less than 10 mm. It is important to note that although the water transport rate improves in the thinner wood, the thermal confinement performance deteriorates with decreasing wood thickness, thus leading to more heat dissipation to the bulk water. The cocobolo wood-based SSGD with a thickness of 50 mm demonstrated a significantly reduced ER, which can be ascribed to an inadequate water supply. According to our theoretical model and experimental results we can conclude that the ER improves with decreasing thickness of the wood-based SSGDs when the thickness is greater than the threshold (defined as T_1 ; see Figure S25B). When taking thermal dissipation into account, the ER of the SSGDs with a thickness smaller than T_1 will be reduced due to the increased heat dissipation and decreased surface temperature. However, the determination of T_1 is complicated and cannot be achieved by any theoretical model. Therefore, further work needs to be done to determine the T_1 values.

EXPERIMENTAL PROCEDURES

Materials

Pine wood was purchased from Woo. Cocobolo, maple, and padauk wood were purchased from Woodcraft Woodshop. Basswood was purchased from Walnut Hollow Company. Elm and locust wood were purchased from Dusty Dog Woodworks. Olive wood was purchased from Holy Land Market. Cedar wood was purchased from Cedar America. Yew wood was purchased from Inlay Accessories. Balsa wood was purchased from Midwest Products Co. Poplar and oak wood were purchased from Home Depot.

Wood-Based SSGD Fabrication

Wood blocks with dimensions of $2 \times 2 \times 1$ cm were obtained by cutting wood vertical to the tree growth direction. Then, the top surface of the wood blocks was heated and carbonized for 60 s on a hot plate at a temperature of 500°C. The same carbonization time was applied to obtain similar carbonized layer thicknesses.

Solar Steam Generation Measurement

The solar steam generation experiment was performed on a custom optical measurement system with a multi-functional solar simulator (Newport Oriel 69,907) and optical components (Newport Oriel 67,005). The wood-based SSGDs were placed in a glass Petri dish filled with enough water. The weight loss was measured by a precision electronic balance (Citizen CX301) with a high precision of 0.1 mg and recorded in real-time using a digital video camera. The surface temperature of the carbonized layer was determined by a thermocouple (Omega HH74K).

Characterizations

The microstructures of the wood samples were determined by a field emission scanning electron microscopy (FESEM, Hitachi SU-70). The light transmittance and reflectance spectra of the wood-based SSGDs were determined using a UV-visible spectrophotometer with an integrated sphere (Lambda 35, PerkinElmer, USA) in the range of 250–2,500 nm wavelength. The absorption spectrum was calculated based on the transmittance and reflectance spectra obtained. The thermal conductivity measurements of the original wood are summarized in the [Supplemental Information](#). The mechanical properties of the wood samples were measured using a tensile testing machine (Tinius Olsen H5KT).

SUPPLEMENTAL INFORMATION

Supplemental Information includes Supplemental Experimental Procedures and 25 figures and can be found with this article online at <https://doi.org/10.1016/j.joule.2017.09.011>.

AUTHOR CONTRIBUTIONS

L.H. and C.J. designed the experiments. Y.L. performed the water extraction experiments. Z.Y. and B.Y. carried out the thermal conductivity characterization. C.J. and F.J. measured the optical and mechanical properties. G.C. and S.D. derived the theoretical model. Y.K. drew the schematics. Y.Y. and H.X. did the SEM characterization. G.P. contributed to revising the paper. All authors commented on the manuscript writing.

ACKNOWLEDGMENTS

C.J. and Y.L. would like to acknowledge the China Scholarship Council (CSC) for financial support. The authors acknowledge Dr. Robert J. Bonenberger in the Department of Materials Science and Engineering at University of Maryland College Park for the mechanical tests. We also acknowledge the support from Maryland NanoCenter and its AIMLab.

Received: May 23, 2017

Revised: July 18, 2017

Accepted: September 22, 2017

Published: November 15, 2017

REFERENCES

1. Plomion, C., Leprovost, G., and Stokes, A. (2001). Wood formation in trees. *Plant Physiol.* 127, 1513–1523.
2. Gibson, L.J. (2012). The hierarchical structure and mechanics of plant materials. *J. R. Soc. Interface* 9, 2749–2766.
3. Jonoobi, M., Oladi, R., Davoudpour, Y., Oksman, K., Dufresne, A., Hamzeh, Y., and Davoodi, R. (2015). Different preparation methods and properties of nanostructured cellulose from various natural resources and residues: a review. *Cellulose* 22, 935–969.
4. Peyre, J., Paakkonen, T., Reza, M., and Kontturi, E. (2015). Simultaneous preparation of cellulose nanocrystals and micron-sized porous colloidal particles of cellulose by TEMPO-mediated oxidation. *Green Chem.* 17, 808–811.
5. Zhang, K., Sun, P., Liu, H., Shang, S., Song, J., and Wang, D. (2016). Extraction and comparison of carboxylated cellulose nanocrystals from bleached sugarcane bagasse pulp using two different oxidation methods. *Carbohydr. Polym.* 138, 237–243.

- Chen, L., Zhu, J.Y., Baez, C., Kitin, P., and Elder, T. (2016). Highly thermal-stable and functional cellulose nanocrystals and nanofibrils produced using fully recyclable organic acids. *Green Chem.* **18**, 3835–3843.
- Jia, C., Chen, L., Shao, Z., Agarwal, U.P., Hu, L., and Zhu, J.Y. (2017). Using a fully recyclable dicarboxylic acid for producing dispersible and thermally stable cellulose nanomaterials from different cellulosic sources. *Cellulose* **24**, 2483–2498.
- Wang, W., Mozuch, M.D., Sabo, R.C., Kersten, P., Zhu, J.Y., and Jin, Y. (2015). Production of cellulose nanofibrils from bleached eucalyptus fibers by hyperthermostable endoglucanase treatment and subsequent microfluidization. *Cellulose* **22**, 351–361.
- Sacui, I.A., Nieuwendaal, R.C., Burnett, D.J., Stranick, S.J., Jorfi, M., Weder, C., Foster, E.J., Olsson, R.T., and Gilman, J.W. (2014). Comparison of the properties of cellulose nanocrystals and cellulose nanofibrils isolated from bacteria, tunicate, and wood processed using acid, enzymatic, mechanical, and oxidative methods. *ACS Appl. Mater. Interfaces* **6**, 6127–6138.
- Zhu, M., Wang, Y., Zhu, S., Xu, L., Jia, C., Dai, J., Song, J., Yao, Y., Wang, Y., Li, Y., et al. (2017). Anisotropic, transparent films with aligned cellulose nanofibers. *Adv. Mater.* **29**, 1606284.
- Jia, C., Li, T., Chen, C., Dai, J., Kierzewski, I.M., Song, J., Li, Y., Yang, C., Wang, C., and Hu, L. (2017). Scalable, anisotropic transparent paper directly from wood for light management in solar cells. *Nano Energy* **36**, 366–373.
- Chen, F., Gong, A.S., Zhu, M., Chen, G., Lacey, S.D., Jiang, F., Li, Y., Wang, Y., Dai, J., Yao, Y., et al. (2017). Mesoporous, three-dimensional wood membrane decorated with nanoparticles for highly efficient water treatment. *ACS Nano* **11**, 4275–4282.
- Chen, C., Zhang, Y., Li, Y., Dai, J., Song, J., Yao, Y., Gong, Y., Kierzewski, I., Xie, J., and Hu, L. (2017). All-wood, low tortuosity, aqueous, biodegradable supercapacitors with ultra-high capacitance. *Energy Environ. Sci.* **10**, 538–545.
- Zhu, M., Li, T., Davis, C.S., Yao, Y., Dai, J., Wang, Y., AlQatari, F., Gilman, J.W., and Hu, L. (2016). Transparent and haze wood composites for highly efficient broadband light management in solar cells. *Nano Energy* **26**, 332–339.
- Xu, X., Zhou, J., Jiang, L., Lubineau, G., Ng, T., Ooi, B.S., Liao, H.Y., Shen, C., Chen, L., and Zhu, J.Y. (2016). Highly transparent, low-haze, hybrid cellulose nanopaper as electrodes for flexible electronics. *Nanoscale* **8**, 12294–12306.
- Jung, Y.H., Chang, T.H., Zhang, H., Yao, C., Zheng, Q., Yang, V.W., Mi, H., Kim, M., Cho, S.J., Park, D.W., et al. (2015). High-performance green flexible electronics based on biodegradable cellulose nanofibril paper. *Nat. Commun.* **6**, 7170.
- Li, T., Zhu, M.W., Yang, Z., Song, J.W., Dai, J.Q., Yao, Y.G., Luo, W., Pastel, G., Yang, B., and Hu, L.B. (2016). Wood composite as an energy efficient building material: guided sunlight transmittance and effective thermal insulation. *Adv. Energy Mater.* **6**, 1601122.
- Carrillo, C.A., Nypeloe, T., and Rojas, O.J. (2016). Double emulsions for the compatibilization of hydrophilic nanocellulose with non-polar polymers and validation in the synthesis of composite fibers. *Soft Matter* **12**, 2721–2728.
- Sharon, H., and Reddy, K.S. (2015). A review of solar energy driven desalination technologies. *Renew. Sust. Energy Rev.* **41**, 1080–1118.
- Zhou, L., Tan, Y., Wang, J., Xu, W., Yuan, Y., Cai, W., Zhu, S., and Zhu, J. (2016). 3D self-assembly of aluminium nanoparticles for plasmon-enhanced solar desalination. *Nat. Photon.* **10**, 393–398.
- Liu, K.K., Jiang, Q., Tadepalli, S., Raliya, R., Biswas, P., Naik, R.R., and Singamaneni, S. (2017). Wood-graphene oxide composite for highly efficient solar steam generation and desalination. *ACS Appl. Mater. Interfaces* **9**, 7675–7681.
- Xue, G., Liu, K., Chen, Q., Yang, P., Li, J., Ding, T., Duan, J., Qi, B., and Zhou, J. (2017). Robust and low-cost flame-treated wood for high-performance solar steam generation. *ACS Appl. Mater. Interfaces* **9**, 15052–15057.
- Tian, L., Luan, J., Liu, K.-K., Jiang, Q., Tadepalli, S., Gupta, M.K., Naik, R.R., and Singamaneni, S. (2016). Plasmonic biofoam: a versatile optically active material. *Nano Lett.* **16**, 609–616.
- Jiang, Q., Tian, L., Liu, K.K., Tadepalli, S., Raliya, R., Biswas, P., Naik, R.R., and Singamaneni, S. (2016). Bilayered biofoam for highly efficient solar steam generation. *Adv. Mater.* **28**, 9400–9407.
- Li, Y., Gao, T., Yang, Z., Chen, C., Luo, W., Song, J., Hitz, E., Jia, C., Zhou, Y., Liu, B., et al. (2017). 3D-Printed, all-in-one evaporator for high-efficiency solar steam generation under 1 sun illumination. *Adv. Mater.* **29**, 1700981.
- Zhou, L., Tan, Y., Ji, D., Zhu, B., Zhang, P., Xu, J., Gan, Q., Yu, Z., and Zhu, J. (2016). Self-assembly of highly efficient, broadband plasmonic absorbers for solar steam generation. *Sci. Adv.* **2**, e1501227.
- Li, X., Lin, R., Ni, G., Xu, N., Hu, X., Zhu, B., Lv, G., Li, J., Zhu, S., and Zhu, J. (2017). Three-dimensional artificial transpiration for efficient solar waste-water treatment. *Natl. Sci. Rev.*, nwx051.
- Li, X., Xu, W., Tang, M., Zhou, L., Zhu, B., Zhu, S., and Zhu, J. (2016). Graphene oxide-based efficient and scalable solar desalination under one sun with a confined 2D water path. *Proc. Natl. Acad. Sci. USA* **113**, 13953–13958.
- O'Sullivan, A.C. (1997). Cellulose: the structure slowly unravels. *Cellulose* **4**, 173–207.
- Scheller, H.V., and Ulvskov, P. (2010). Hemicelluloses. *Annu. Rev. Plant Biol.* **61**, 263–289.
- Boerjan, W., Ralph, J., and Baucher, M. (2003). Lignin biosynthesis. *Annu. Rev. Plant Biol.* **54**, 519–546.
- Rogers, L.A., and Campbell, M.M. (2004). The genetic control of lignin deposition during plant growth and development. *New Phytol.* **164**, 17–30.
- Wang, Y., Zhang, L., and Wang, P. (2016). Self-floating carbon nanotube membrane on macroporous silica substrate for highly efficient solar-driven interfacial water evaporation. *ACS Sustain. Chem. Eng.* **4**, 1223–1230.
- Vay, O., De Borst, K., Hansmann, C., Teischinger, A., and Mueller, U. (2015). Thermal conductivity of wood at angles to the principal anatomical directions. *Wood Sci. Technol.* **49**, 577–589.
- Hu, X., Xu, W., Zhou, L., Tan, Y., Wang, Y., Zhu, S., and Zhu, J. (2017). Tailoring graphene oxide-based aerogels for efficient solar steam generation under one sun. *Adv. Mater.* **29**, 1604031.
- Ghasemi, H., Ni, G., Marconnet, A.M., Loomis, J., Yerci, S., Miljkovic, N., and Chen, G. (2014). Solar steam generation by heat localization. *Nat. Commun.* **5**, 4449.